

# Symmetry-Mismatch-Induced Ferromagnetism in the Interfacial Layers of CaRuO<sub>3</sub>/SrTiO<sub>3</sub> Superlattices

Wenxiao Shi, Jine Zhang, Xiaobing Chen, Qinghua Zhang, Xiaozhi Zhan, Zhe Li, Jie Zheng, Mengqin Wang, Furong Han, Hui Zhang, Lin Gu, Tao Zhu, Banggui Liu, Yunzhong Chen, Fengxia Hu, Baogen Shen, Yuansha Chen,\* and Jirong Sun\*

By modifying the entangled multi-degrees of freedom of transition-metal oxides, interlayer coupling usually produces interfacial phases with unusual functionalities. Herein, a symmetry-mismatch-driven interfacial phase transition from paramagnetic to ferromagnetic state is reported. By constructing superlattices using CaRuO<sub>3</sub> and SrTiO<sub>3</sub>, two oxides with different oxygen octahedron networks, the tilting/rotation of oxygen octahedra near interface is tuned dramatically, causing an angle increase from  $\approx 150^\circ$  to  $\approx 165^\circ$  for the Ru–O–Ru bond. This in turn drives the interfacial layer of CaRuO<sub>3</sub>,  $\approx 3$  unit cells in thickness, from paramagnetic into ferromagnetic state. The ferromagnetic order is robust, showing the highest Curie temperature of  $\approx 120$  K and the largest saturation magnetization of  $\approx 0.7 \mu_B$  per formula unit. Density functional theory calculations show that the reduced tilting/rotation of RuO<sub>6</sub> octahedra favors an itinerant ferromagnetic ground state. This work demonstrates an effective phase tuning by coupled octahedral rotations, offering a new approach to explore emergent materials with desired functionalities.

as high- $T_C$  superconductivity, colossal magnetoresistance, ferromagnetism, ferroelectricity, and multiferroicity.<sup>[1–6]</sup> In particular, when grouping different oxides into heterostructures or superlattices (SLs), the interlayer coupling sometimes strongly modifies the multi-degrees of freedom, generating distinct interfacial phases with unforeseen functionalities.<sup>[7–13]</sup> For example, paramagnetic (PM) LaNiO<sub>3</sub> becomes helical antiferromagnetic when forming a SL with LaMnO<sub>3</sub>, yielding a magnetic pinning to neighboring LaMnO<sub>3</sub>.<sup>[14,15]</sup> In contrast, PM NdNiO<sub>3</sub> becomes ferromagnetic (FM) when sandwiched by La<sub>0.67</sub>Sr<sub>0.33</sub>MnO<sub>3</sub> layers.<sup>[16]</sup> Interfacial FM also emerges in the PM SrIrO<sub>3</sub> layer in proximity to the La<sub>0.7</sub>Sr<sub>0.3</sub>MnO<sub>3</sub> or LaCoO<sub>3</sub> FM layers.<sup>[17–19]</sup> These results are usually understood by the concept of

magnetic proximity effect: when two oxides are in close contact, the hybridization of adjacent atomic orbitals produces low-lying molecular orbits thus interlayer charge transfer and exchange interaction according to the Goodenough–Kanamori–Anderson

## 1. Introduction

The strong interplay of multi-degrees of freedom in perovskite oxides has led to a wide variety of intriguing properties, such

W. Shi, X. Chen, Q. Zhang, Z. Li, J. Zheng, M. Wang, L. Gu, T. Zhu, B. Liu, Y. Chen, F. Hu, B. Shen, Y. Chen, J. Sun  
Beijing National Laboratory for Condensed Matter Physics and Institute of Physics

Chinese Academy of Sciences  
Beijing 100190, China

E-mail: yschen@iphy.ac.cn; jrsun@iphy.ac.cn

W. Shi, Q. Zhang, Z. Li, J. Zheng, M. Wang, L. Gu, B. Liu, Y. Chen, F. Hu, B. Shen, Y. Chen, J. Sun  
School of Physical Sciences  
University of Chinese Academy of Sciences  
Beijing 100049, China

J. Zhang, F. Han, H. Zhang  
School of Integrated Circuit Science and Engineering  
Beihang University  
Beijing 100191, China

X. Chen  
Shenzhen Institute for Quantum Science and Engineering (SIQSE) and Department of Physics  
Southern University of Science and Technology  
Shenzhen 518055, China


X. Zhan, T. Zhu  
Spallation Neutron Source Science Center  
Dongguan, Guangdong 523803, China

B. Shen  
Ningbo Institute of Materials Technology & Engineering  
Chinese Academy of Sciences  
Ningbo, Zhejiang 315201, China

Y. Chen  
Fujian Innovation Academy  
Chinese Academy of Sciences  
Fuzhou, Fujian 350108, China

J. Sun  
Spintronics Institute  
University of Jinan  
Jinan, Shandong 250022, China

J. Sun  
Songshan Lake Materials Laboratory  
Dongguan, Guangdong 523808, China

 The ORCID identification number(s) for the author(s) of this article can be found under <https://doi.org/10.1002/adfm.202300338>.

DOI: 10.1002/adfm.202300338

rules,<sup>[20–22]</sup> transferring magnetic order from FM layer to adjacent layers. All these works indicate that the interface engineering is a powerful tool for tuning the properties of perovskite oxides.

The 4d ruthenate SrRuO<sub>3</sub> (SRO) has received intensive research attention owing to its fascinating itinerant FM and rich properties associated topological spin texture.<sup>[23–27]</sup> As a sister material of SRO, CaRuO<sub>3</sub> (CRO) has the same GdFeO<sub>3</sub>-typed orthorhombic structure with *Pbnm* symmetry.<sup>[28–30]</sup> However, due to the larger orthorhombic distortion of the RuO<sub>6</sub> octahedra, CRO maintains the nonmagnetic metal behavior to at least 2 K in either bulk or thin film form.<sup>[31–36]</sup> Here we report on symmetry-mismatch-induced FM in the interfacial layers of the CaRuO<sub>3</sub>/SrTiO<sub>3</sub> (CRO/STO) SLs on either (LaAlO<sub>3</sub>)<sub>0.3</sub>(SrAl<sub>0.5</sub>Ta<sub>0.5</sub>O<sub>3</sub>)<sub>0.7</sub> (LSAT) or STO substrates. By combining PM CRO and diamagnetic STO, two oxides with distinct symmetries and oxygen octahedron arrays,<sup>[28–30]</sup> we can effectively tune the tilting/rotation of RuO<sub>6</sub> octahedra at CRO/STO interface, causing an angle increase from ≈150° to ≈165° for Ru–O–Ru bond. This in turn drives the interfacial CRO layer of ≈3 unit cells (uc) from PM to FM state. The FM order is robust, showing the highest Curie temperature (*T*<sub>C</sub>) of ≈120 K and the largest saturation magnetization (*M*<sub>S</sub>) of ≈0.7 μ<sub>B</sub> per formula unit (f.u.), regardless of substrate strains. According to results of density functional theory (DFT) calcu-

lations, the reduced RuO<sub>6</sub> octahedra tilting/rotation causes an increase in density of states (DOS) near Fermi surface, favoring the itinerant FM state according to the Stoner model.<sup>[37]</sup> This work demonstrates an effective tuning of magnetic ground state by coupled octahedral rotations at symmetry-mismatched heterointerfaces.

## 2. Results and Discussion

### 2.1. Structural Analysis

(CRO<sub>*n*</sub>/STO<sub>1</sub>)<sub>10</sub> SLs composed of alternately stacked CRO (*n* uc) and STO (1 uc) layers with 10 repetitions were epitaxially grown on (001)-oriented LSAT or STO substrates (see Figure S1, Supporting Information). Figure 1a,b shows the X-ray diffraction (XRD) spectra of the SLs. The thickness fringes around (001) peak indicate good crystallinity and smooth surface of the samples. Distinct satellite peaks are further detected, shifting toward (001) main peak as *n* increases, which is a general feature of the SL XRD spectra. To determine the in-plane strain state of the SLs, the reciprocal space mapping (RSM) of the (103) reflection is further measured. Take (CRO<sub>10</sub>/STO<sub>1</sub>)<sub>10</sub> as an example. The diffraction spots of the SL (marked by red arrows) locate just below (Figure 1c) or above (Figure 1d) that

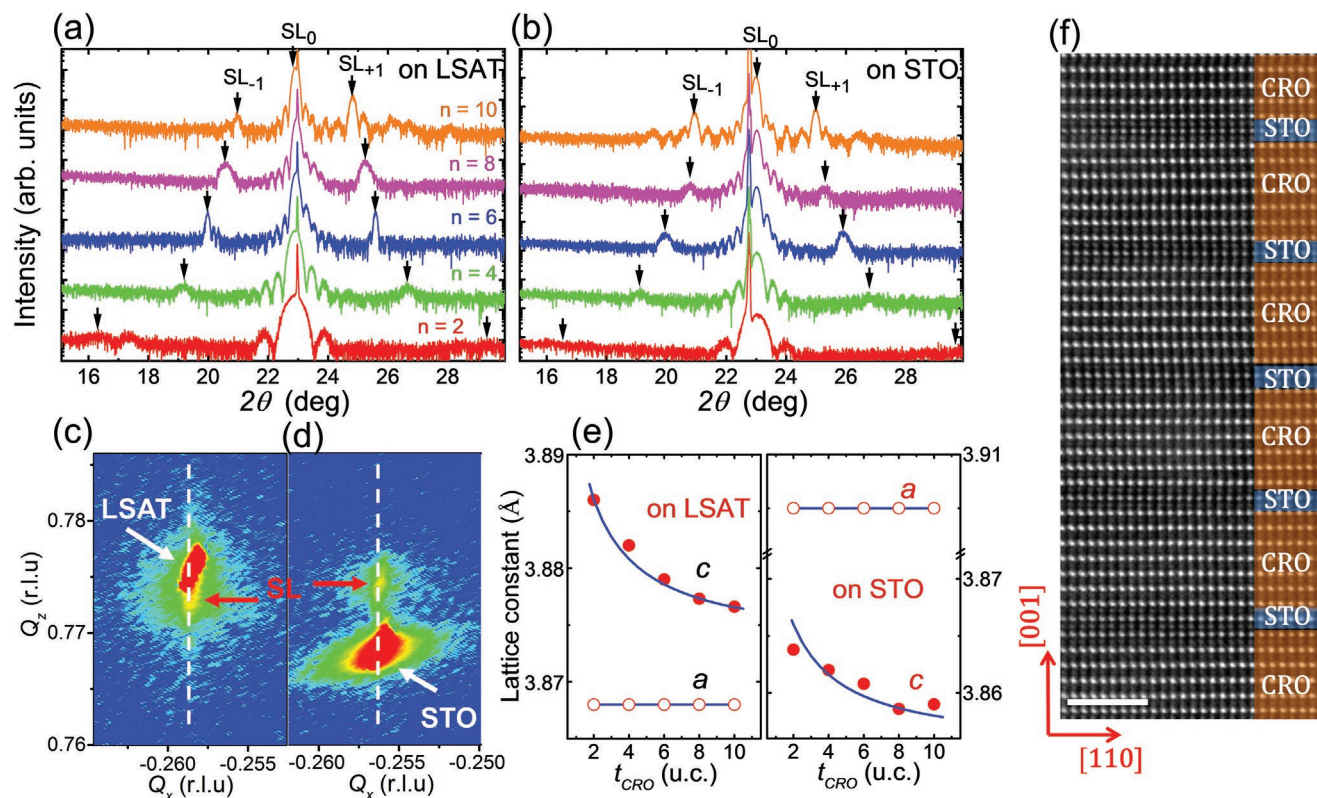


**Figure 1.** a) High-resolution  $\theta$ - $2\theta$  patterns around (001) peak for (CRO<sub>*n*</sub>/STO<sub>1</sub>)<sub>10</sub> SLs on LSAT and b) STO. SL<sub>0</sub> indicates (001) main peak and SL<sub>-1</sub>, SL<sub>+1</sub> indicate satellite peaks. c) RSM around (103) reflection for (CRO<sub>10</sub>/STO<sub>1</sub>)<sub>10</sub> SL on LSAT and d) STO. e) Out-of-plane and in-plane lattice constants as functions of CRO layer thickness, deduced from the XRD and RSM results for the SLs on LSAT (left panel) or STO (right panel) substrate. The blue lines are calculated out-of-plane lattice constants adopting the formula  $c = (n \times c_{\text{CRO}} + c_{\text{STO}}) / (n + 1)$ , where  $c_{\text{STO}}$  and  $c_{\text{CRO}}$  represent the *c*-axis lattice constants of STO and CRO sublayers. f) HAADF image of the (CRO<sub>7</sub>/STO<sub>1</sub>)<sub>10</sub> SL on LSAT substrate, recorded along the [110] zone axis by STEM. The locations of CRO and STO layers are marked by brown and blue color. Scale bar marks a length of 2 nm.

of the substrate, i.e., the SL is coherently strained to substrate, without in-plane lattice relaxation. This conclusion is also applicable to other samples. The  $a$ - and  $c$ -axis lattice constants of the SLs are further deduced and shown in Figure 1e. The dependence of effective  $c$  on CRO layer thickness can be well described by the formula  $c = (n \times c_{\text{CRO}} + c_{\text{STO}})/(n + 1)$ , where  $c_{\text{STO}}$  and  $c_{\text{CRO}}$  represent the  $c$ -axis lattice constants of the STO and CRO sublayers, respectively. Since CRO has a smaller lattice constant as compared to STO (3.850 vs. 3.905 Å), the  $c$ -axis constant of the SLs displays a smooth decrease as  $n$  increases. As reported, the bulk phase of CRO is orthorhombic, with the lattice constants of  $a_0 = 5.362$ ,  $b_0 = 5.541$ , and  $c_0 = 7.686$  Å.<sup>[28–30]</sup> Alternatively, it can be described by a pseudo-cubic phase with a lattice parameter of 3.850 Å.

To get the information on atomic arrangements, the lattice structure of the SLs is further investigated by the high-resolution scanning transmission electron microscope (STEM). Figure 1f presents the high-angle annular dark-field (HAADF) lattice image of the cross-section of  $(\text{CRO}_7/\text{STO}_1)_{10}$  SL, recorded along the  $[\bar{1}\bar{1}0]$  zone axis. The strong light contrast between Ru and Ti ions confirms that the STO monolayer is well sandwiched by the CRO layers. The electron energy loss spectra further imply that Sr/Ca intermixing may take place for interfacial A-sites, while the Ru/Ti intermixing at interfacial B-sites is negligibly small (see Figure S2, Supporting Information).

## 2.2. Emergent Ferromagnetism in CRO/STO SLs

To explore the effect of interface engineering, the transport properties of  $(\text{CRO}_n/\text{STO}_1)_{10}$  SLs are investigated. Figure 2a

shows the temperature dependence of longitudinal resistivity ( $\rho_{xx}$ ) for the SLs on LSAT. The  $\rho_{xx}$ - $T$  relation of a CRO bare film ( $\approx 50$  uc) is also presented for comparison. As expected, SLs with thick CRO sublayers are metallic except for the low temperature region where a slight resistive upturn takes place. With the decrease of the thickness of CRO layer ( $t_{\text{CRO}}$ ), the metallic  $\rho_{xx}$ - $T$  dependence turns to semiconducting dependence. Noting that the CRO bare film is well metallic and STO is strongly insulating, the transport behavior of SLs is actually dominated by the CRO sublayers. The enhanced resistivity could be a special feature of the CRO ultrathin sublayers, due to the interlayer coupling between STO and CRO.

Further experiments reveal more important properties of CRO sublayers. As a function of magnetic field ( $H$ ), in Figure 2b we show the anomalous Hall resistivity ( $\rho_{xy}^{\text{AHE}}$ ) collected at different temperatures for the typical SL of  $(\text{CRO}_6/\text{STO}_1)_{10}$ . Remarkably, clear  $\rho_{xy}^{\text{AHE}}$ - $H$  hysteresis loops are observed at temperatures  $< 20$  K. Although the magnetic hysteresis disappears at the temperatures  $\geq 50$  K, AHE remains visible when  $T = 100$  K. These results strongly suggest the emergence of FM order in the CRO sublayers. The saturation value of  $\rho_{xy}^{\text{AHE}}$  (extrapolating the  $\rho_{xy}^{\text{AHE}}$ - $H$  curve to the magnetic field of 10 T) is  $\approx 2.5$   $\mu\Omega$  cm at 2 K, and decreases with the increase of temperature. In addition, the  $\rho_{xy}^{\text{AHE}}$ - $H$  curve demonstrates a large coercivity field ( $H_C$ ), as high as  $\approx 2.3$  T at 2 K. Although  $H_C$  decreases sharply after heating, it remains sizable when  $T = 20$  K.

It is worth noting that the FM order is a generic feature of all  $(\text{CRO}_n/\text{STO}_1)_{10}$  SLs. Figure 2c compares the  $\rho_{xy}^{\text{AHE}}$ - $H$  loops at 2 K for different samples. The highest  $\rho_{xy}^{\text{AHE}}$  ( $\approx 3.1$   $\mu\Omega$  cm) appears in the SL with the thinnest CRO sublayers (2 uc).

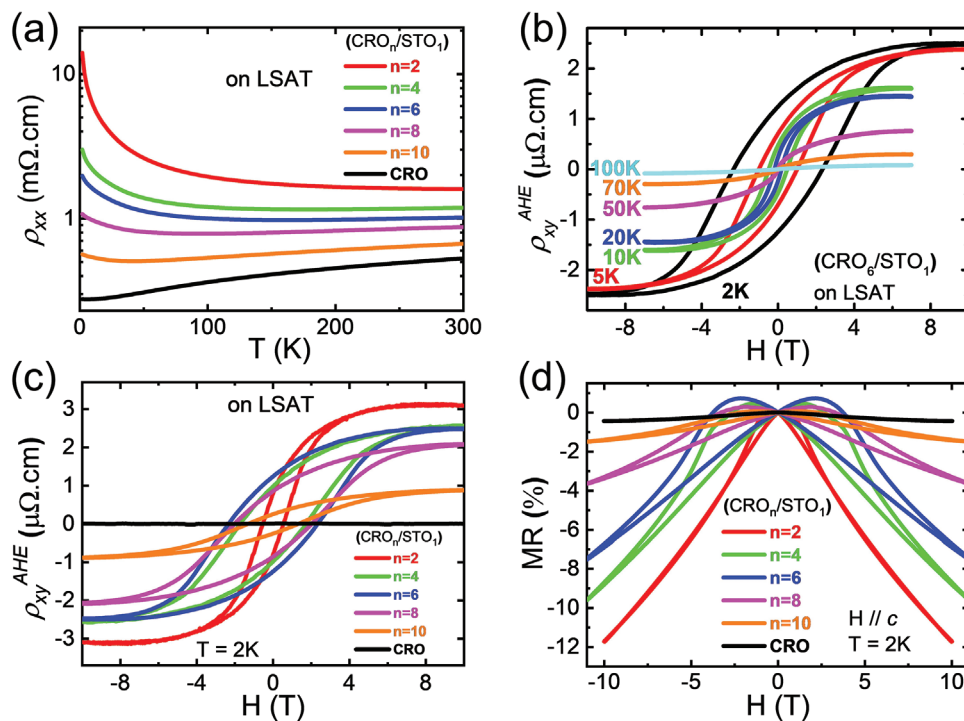


**Figure 2.** a)  $\rho_{xx}$ - $T$  curves of  $(\text{CRO}_n/\text{STO}_1)_{10}$  SLs on LSAT substrates. The corresponding data of a bare CRO film (50 uc in thickness) is also presented for comparison. b)  $\rho_{xy}^{\text{AHE}}$ - $H$  curves of  $(\text{CRO}_6/\text{STO}_1)_{10}$  SL measured from 2 to 100 K. c)  $\rho_{xy}^{\text{AHE}}$ - $H$  and d) MR- $H$  curves at 2 K for  $(\text{CRO}_n/\text{STO}_1)_{10}$  SLs on LSAT.



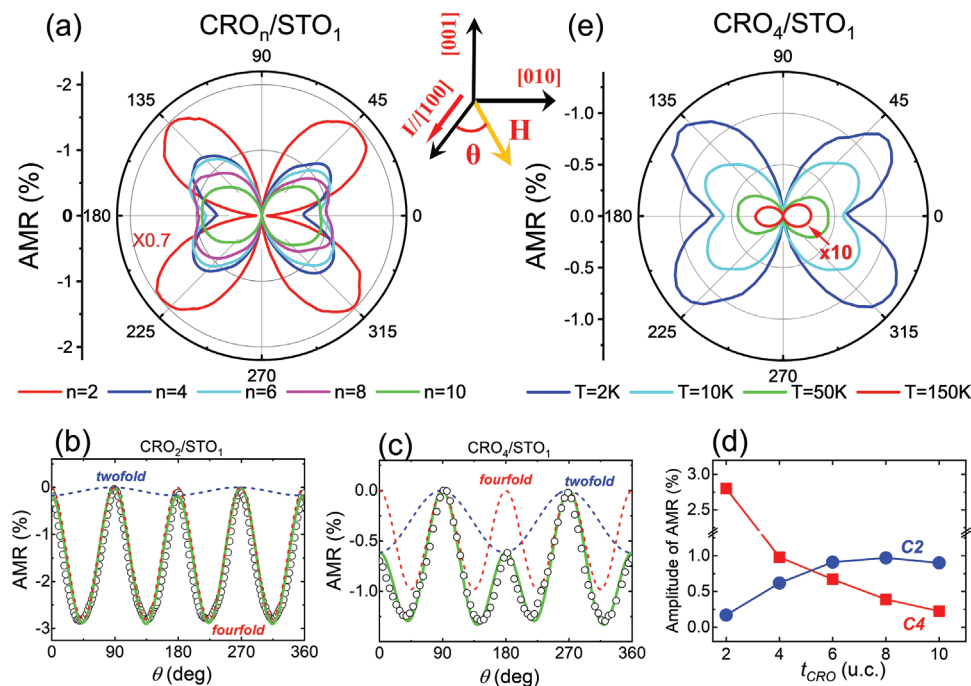


**Figure 3.** a) Polar plots of in-plane AMR for  $(\text{CRO}_n/\text{STO}_1)_{10}$  SLs at 2 K and 10 T. Inset is the geometry for AMR measurements. The electric current is applied along the  $[100]$  direction and the magnetic field is rotated in the  $(001)$  plane, forming an angle of  $\theta$  with applied current. b) Corresponding angle dependent AMR for  $(\text{CRO}_2/\text{STO}_1)_{10}$  and c)  $(\text{CRO}_4/\text{STO}_1)_{10}$  SLs. Black symbols are experimental data. Green lines are the results of curve fitting. Red and blue lines are fourfold and twofold components, respectively. d) Polar plots of the AMR of the  $(\text{CRO}_4/\text{STO}_1)_{10}$  SLs measured at different temperatures ranging from 2 to 150 K. e) Layer thickness dependence of the amplitudes of the fourfold AMR (red symbols) and the twofold AMR (blue symbols).

Although  $\rho_{xy}^{\text{AHE}}$  exhibits a monotonic decrease, it remains sizable ( $\approx 0.9 \mu\Omega \text{ cm}$ ) when  $t_{\text{CRO}}$  increases to 10 uc. In contrast, the CRO bare film shows no AHE signal at all. Similar trend is identified from the magnetoresistance (MR) results. Figure 2d depicts the magnetic field dependence of the  $\text{MR} = (R_{\text{H}} - R_0)/R_0$  obtained at 2 K, where  $R_0$  and  $R_{\text{H}}$  are the longitudinal resistances measured without and with an out-of-plane field, respectively. Butterfly-shaped MR- $H$  loops with two broad peaks at  $\pm H_{\text{C}}$  are clearly seen for the SLs. This feature indicates the presence of magnetic domains: it is the reconstruction of magnetic domains that results in the MR peaks. The MR value, recorded at 10 T and 2 K, gradually decreases from  $-11.7\%$  for  $n = 2$  to  $-1.4\%$  for  $n = 10$ . All these features suggest that the ferromagnetism exists only in the near interface region, i.e., the STO monolayer has driven its CRO neighbors from the PM into the FM state. This is unusual since neither STO nor CRO has a FM bulk phase.

To get the knowledge about the interfacial phase, the in-plane angle-dependent MR was further investigated for the  $(\text{CRO}_n/\text{STO}_1)_{10}$  SLs. The anisotropic MR is defined by  $\text{AMR} = (R_{\theta} - R_{90^\circ})/R_{90^\circ}$ , where  $R_{\theta}$  is the resistance measured with an in-plane field forming an angle of  $\theta$  with the current applied along  $[100]$ . Figure 3a is the AMR polar plots for different SLs at 2 K. For clarity, the angular dependence of the AMR is also shown for two typical samples (Figure 3b,c). Apparently, the AMR of  $(\text{CRO}_2/\text{STO}_1)_{10}$ , which is highly polarized as will be seen later, mainly exhibits a fourfold-symmetry with four valleys in the  $\langle 110 \rangle$  directions and four peaks in the  $\langle 100 \rangle$  directions. This fourfold-symmetry may be a fingerprint of the FM phase.<sup>[38]</sup> It suggests that the magnetic easy axis of the CRO sublayers lies

along the  $\langle 110 \rangle$  directions, where the AMR valley appear due to the minimal spin-flip scattering when spins are fully align along applied field.<sup>[19,39]</sup> An additional oscillation with twofold-symmetry develops when  $t_{\text{CRO}} \geq 4$  uc, leading to an evolution of AMR symmetry from fourfold to twofold as  $t_{\text{CRO}}$  increases. Similar AMR with two components has been reported in previous literature, and the twofold component is usually ascribed to normal AMR or Lorentz scattering.<sup>[40,41]</sup> This conclusion is further confirmed by the temperature dependence of the AMR (Figure 3d), which shows, for  $(\text{CRO}_4/\text{STO}_1)_{10}$ , mixed fourfold and twofold oscillations at low temperatures and a twofold oscillation when  $T > T_{\text{C}}$ . The experimental data can be well described by the formula  $\text{AMR} = c_2 \times \cos(2\theta - \omega_2) + c_4 \times \cos(4\theta - \omega_4)$ , where  $c_2$  and  $c_4$  are the amplitudes of twofold and fourfold oscillations, respectively, and  $\omega_2$  and  $\omega_4$  are the corresponding offset angles. Satisfactory agreement with experiment results is obtained adopting suitable fitting parameters (Figure 3b,c; Figure S3, Supporting Information). Figure 3e illustrates the  $c_2$ - $t_{\text{CRO}}$  and  $c_4$ - $t_{\text{CRO}}$  relations, demonstrating the evolution of the two kinds of AMRs with the layer thickness of CRO. The fourfold AMR displays a continuous decrease with increased  $t_{\text{CRO}}$ , whereas the twofold AMR rapidly increases to a saturation value of  $-1\%$  (Figure 3e; Figure S3, Supporting Information).

In previous works, theoretical calculations have predicted a FM ground state in CRO films under large tensile epitaxial strains of 2%–4%.<sup>[42]</sup> However, the experimental results are controversial.<sup>[31–36,43,44]</sup> For the same CRO film on STO (with a tensile strain of 1.4%), some works reported a weak FM phase,<sup>[43,44]</sup> while others showed the absence of long-range magnetic order.<sup>[31–33]</sup> The robust FM order observed here in the

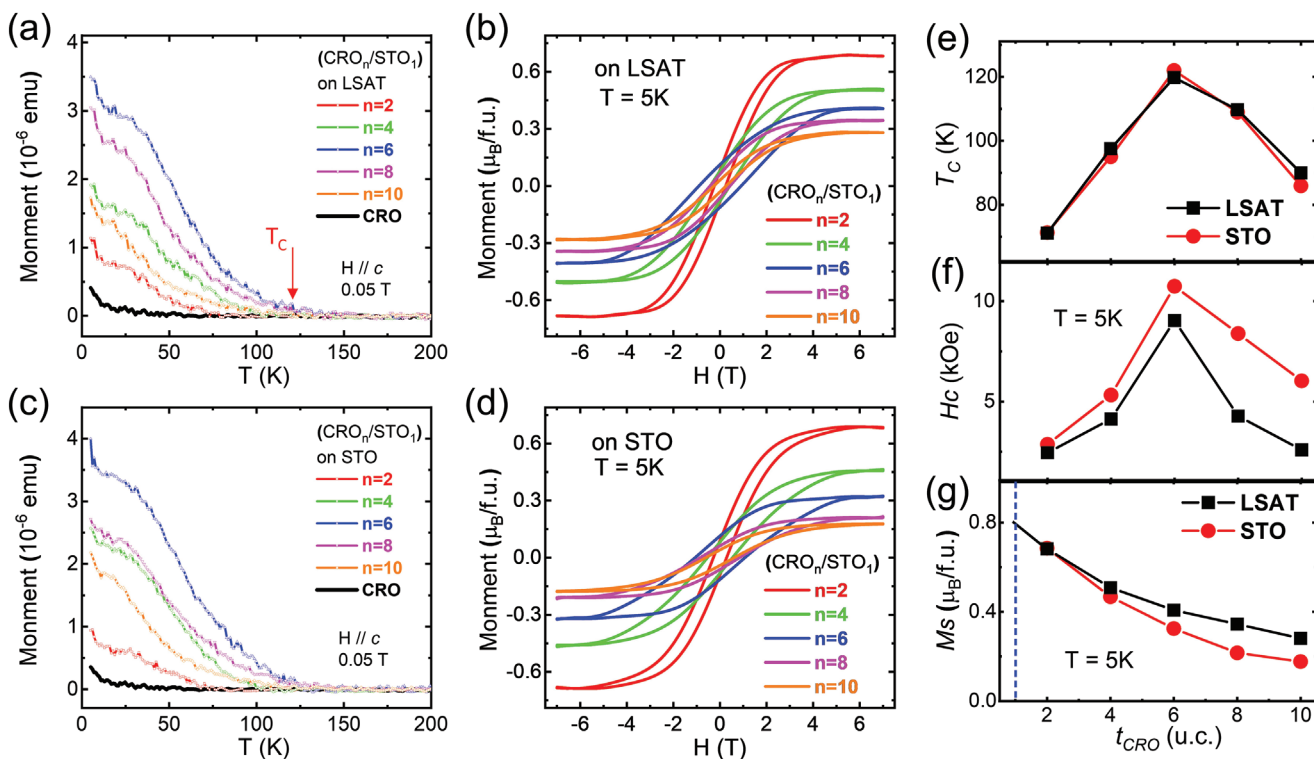


**Figure 4.** a)  $M$ - $T$  curves for  $(\text{CRO}_n/\text{STO}_1)_{10}$  SLs on LSAT, measured with an out-of-plane field of 0.05 T in field-cooling mode. Result for a bare CRO film (50 uc in thickness) is also given for comparison. Red arrow marks Curie temperature. b)  $M$ - $H$  curves for  $(\text{CRO}_n/\text{STO}_1)_{10}$  SLs on LSAT, showing clear magnetic hysteresis loops. c)  $M$ - $T$  and d)  $M$ - $H$  curves for  $(\text{CRO}_n/\text{STO}_1)_{10}$  SLs on the STO substrate. e)  $T_C$ , f)  $H_C$  and g)  $M_s$  as a function of  $t_{\text{CRO}}$  for SLs on LSAT (black symbols) or STO (red symbols).

$(\text{CRO}_n/\text{STO}_1)_{10}$  SLs is unlikely to be caused by strain effect. We found that a CRO bare film on LSAT did not show any features of FM ordering. This may be ascribed to the negligible strain from the LSAT substrate ( $\approx 0.4\%$ ). To further clarify the influence of substrate strain, the transport properties of the SLs grown on the STO substrate are also investigated. They show essentially the same FM features as those observed on LSAT (see Figure S4, Supporting Information), i.e., the clear AHE hysteresis loops and the butterfly-shaped MR. As will be shown later, the SLs on LSAT and STO with the same CRO layer thickness possess basically identical Curie temperature  $T_C$  and saturation moment  $M_s$ . That is to say, the interface ferromagnetism induced in the CRO/STO heterostructure is general, independent of the strain in the SLs. A deeper understanding on such interface engineering on the magnetic ground state of CRO is still imperative, which may reveal a more fundamental approach for developing emergent properties in perovskite ruthenates.

Further evidences of ferromagnetism in  $(\text{CRO}_n/\text{STO}_1)_{10}$  SLs are obtained by direct magnetic measurements. Figure 4a shows the temperature dependence of magnetization ( $M$ - $T$ ) for the SLs on LSAT. Unlike that of the PM CRO bare film, the magnetization of the SL displays a rapid increase upon cooling below  $T_C$  and a smooth tendency toward saturation when temperature is low enough, signifying the PM-to-FM transition. Figure 4b shows the magnetic field dependence of magnetization ( $M$ - $H$ ), recorded at 5 K. Magnetic hysteresis loops are clearly observed for all SLs, confirming the establishment of

FM order. The magnetic results of SLs on STO are also given in Figure 4c,d, which show essentially the same features as that of the SLs on LSAT. The dependence of  $T_C$ ,  $H_C$ , and  $M_s$  on  $t_{\text{CRO}}$  is compared in Figure 4e-g. Here, the  $T_C$  is defined by the zero-crossing temperature of the tangent line (see Figure S5, Supporting Information). It displays a strong dependence on  $t_{\text{CRO}}$ , first increasing and then decreasing as  $t_{\text{CRO}}$  grows from 2 to 10 uc. The maximal  $T_C$  of  $\approx 120$  K occurs in the  $(\text{CRO}_6/\text{STO}_1)_{10}$  SL on either LSAT or STO substrate, which is fairly high noting that it is only  $\approx 150$  K for SRO.<sup>[23-25]</sup> In principle,  $T_C$  is jointly determined by dimensionality and exchange energy. It will be low for ultrathin SL due to reduced dimensionality. As  $t_{\text{CRO}}$  grows, an increase-to-decrease crossover is expected for  $T_C$  as a result of the competition between increased dimensionality and decreased exchange energy. As revealed in Figure S2 (Supporting Information), the nearest  $\text{RuO}_2$  plane is sandwiched between a CaO plane and a (Ca,Sr)O plane at the CRO/STO interface, which may cause a  $\text{Sr}_\delta$ -doping effect to the nearest neighboring CRO layer.<sup>[33]</sup> However, the increase-to-decrease crossover of  $T_C$  versus  $t_{\text{CRO}}$  definitely excludes the  $\text{Sr}_\delta$ -doping effect as the main reason for the emergent FM state observed here. First, the highest  $T_C$  always occurs in the case of  $t_{\text{CRO}} = 6$  uc rather than in the case of  $t_{\text{CRO}} = 2$  uc for which the strongest  $\text{Sr}_\delta$ -doping effect is naturally expected. Second, the maximal  $T_C$  of  $\approx 120$  K is much higher than that obtained by the effect of  $\text{Sr}_\delta$ -doping. For example,  $T_C$  is lower than 50 K for  $\text{Ca}_{0.5}\text{Sr}_{0.5}\text{RuO}_3$  which has a Sr-doping as high as 50%.<sup>[31,36]</sup> The  $H_C$  of SLs also demonstrates a non-monotonic

dependence on  $t_{\text{CRO}}$ , with the maximal value occurred in the case of  $t_{\text{CRO}} = 6$  uc. For the same  $t_{\text{CRO}}$ , the  $H_C$  of samples on LSAT, which is consistent with the results of the Hall effect as presented above. Unlike  $T_C$  and  $H_C$ , the  $M_S$  of the SLs on LSAT (or STO) displays a monotonic decrease with increased  $t_{\text{CRO}}$ , varying from  $\approx 0.7 \mu_B \text{ f.u.}^{-1}$  for  $t_{\text{CRO}} = 2$  uc to  $\approx 0.3 \mu_B \text{ f.u.}^{-1}$  (or  $\approx 0.2 \mu_B \text{ f.u.}^{-1}$ ) for  $t_{\text{CRO}} = 10$  uc. This is the typical feature of interfacial effect, suggesting that the near interface region of CRO is highly polarized compared with distant regions. In addition, though the SLs on STO suffer from a large tensile strain, its  $M_S$  is slightly reduced compared with that of the SLs on LSAT. This result further indicates that the emergent FM state at the CRO/STO interface cannot be simply ascribed to the tensile-strain-induced FM order suggested by previous theoretical calculations.

### 2.3. Lattice Distortions at CRO/STO Interface

Above results reveal the striking difference between interface and bulk phases of CRO. According to the literature,<sup>[28–30]</sup> bulk CRO has a  $\text{GdFeO}_3$ -typed orthorhombic structure with  $Pbnm$  symmetry. Its  $\text{RuO}_6$  octahedron tilts/rotates in the manner of  $a^-c^+$  in Glazer notation,<sup>[45]</sup> causing a large bending of  $\text{Ru-O-Ru}$  bond angle ( $\approx 150^\circ$ ).<sup>[46–48]</sup> In contrast, bulk STO is cubic with a  $pm3m$  symmetry and its  $\text{TiO}_6$  octahedron does not tilt/rotate, showing an ideal  $180^\circ$   $\text{Ti-O-Ti}$  bond angle. To achieve an epitaxial growth, CRO and STO have to adjust the tilting/rotation of their respective oxygen octahedra via the shared apical oxygen ions. Though STO layer is only one

uc in thickness, it may also significantly change the coupled octahedral connections at interface, generating interfacial phases with unique physical properties.<sup>[49–51]</sup> To reveal the oxygen octahedral arrangement at interface, **Figure 5a** gives the annular bright-field (ABF) lattice image of  $(\text{CRO}_8/\text{STO}_1)_{10}$  SL, recorded along  $[1\bar{1}0]$  zone axis. The dark dots correspond to the B-site atoms (Ru and Ti). The A-site atoms (Ca and Sr) lie between the B-sites along  $[001]$  direction. The faint dots represent for O atoms. Since the apical oxygen atoms and A-site atoms partially overlap, we mainly focus on the four corner oxygen of the octahedra. In the case without octahedral tilting/rotation, the corner oxygen will locate at exactly the middle position of the left and right two B-site atoms. Viewing the B-site atomic chain along  $[110]$  direction, it is clear that the corner oxygen moves alternately up and down, indicating the tilting of oxygen octahedra. This feature is observed in either CRO sublayers or STO monolayers. To estimate the degree of the octahedral tilting/rotation, the layer-by-layer variation in  $\text{Ru-O-Ru}$  and  $\text{Ti-O-Ti}$  bond angles obtained by an average of 20 unit cells per layer is shown in **Figure 5b**. As expected, the octahedral tilting in CRO sublayers close to interface is significantly suppressed by the STO spacer. Starting from interface, the  $\beta_{\text{Ru-O-Ru}}$  angles are  $\approx 165^\circ$ ,  $\approx 164^\circ$ , and  $\approx 162^\circ$  in the first, second, and third layers, respectively, significantly larger than that in bulk CRO ( $\approx 150^\circ$ ). Notably, the bond angles of interfacial CRO layers are close to that of SRO ( $\approx 163^\circ$ ), a typical itinerant ferromagnet. A natural inference is that there may be a relation between the octahedral tilting/rotation and the FM order in CRO. An abrupt decline to  $\beta_{\text{Ru-O-Ru}} = 155^\circ$  occurs in the fourth CRO layer, showing a tendency toward bulk phase. This implies that each STO layer can significantly modify three

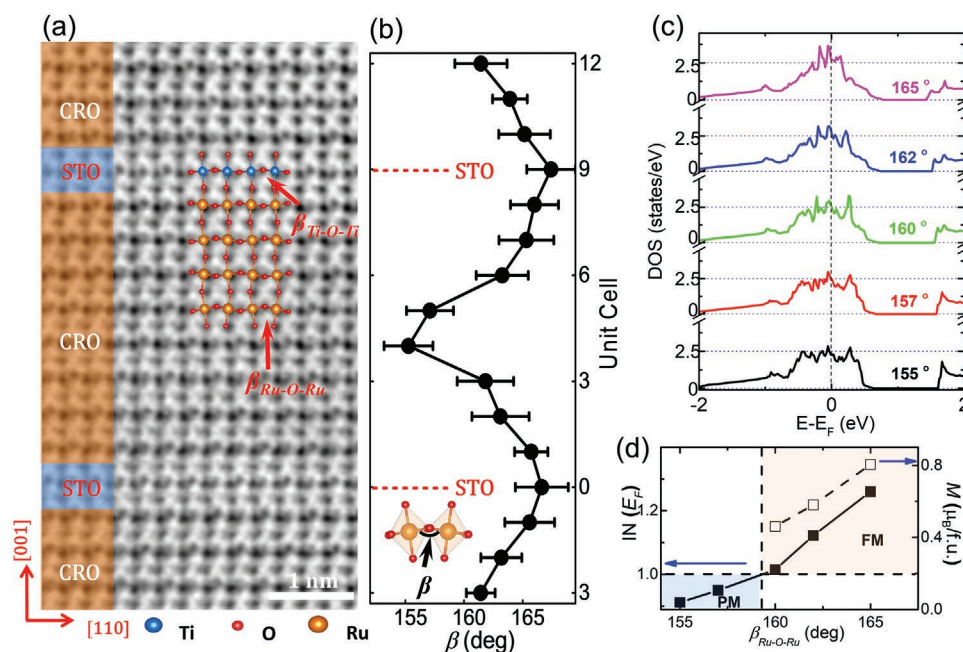


**Figure 5.** a) ABF image of the cross-section of  $(\text{CRO}_8/\text{STO}_1)_{10}$  SL on LSAT. To clearly show octahedral tilting, the networks of  $\text{RuO}_6$  and  $\text{TiO}_6$  octahedra are superimposed on the image. b) Layer-dependent of tilting angle  $\beta_{\text{B-O-B}}$  by averaging 20 unit cells along  $[110]$  direction, where B represents Ti or Ru for different layers. c) DOS generated from DFT calculations for model CRO on LSAT. The vertical dashed line marks the Fermi level. d) Calculated Stoner criterion and effective magnetization as a function of  $\beta_{\text{Ru-O-Ru}}$ . Blue and yellow colors mark the PM and FM regions, respectively.



adjacent CRO layers, i.e., the thickness of interfacial phase is  $\approx 3$  uc. Therefore, PM state may be restored in the intermediate layers when  $t_{\text{CRO}}$  exceeds 6 uc, blocking the magnetic interaction between top and bottom interfacial FM layers. The occurrence of the highest  $T_{\text{C}}$  in  $(\text{CRO}_6/\text{STO}_1)_{10}$  SL may not be by chance. Notably, a  $\text{TiO}_6$  tilting/rotation also takes place for the STO monolayers ( $\beta_{\text{Ti-O-Ti}}$  is  $\approx 167^\circ$  rather than  $180^\circ$ ), resulting in orthorhombic STO. Fortunately, this will not influence the magnetic property of STO since the  $\text{Ti}^{4+}$  has a vanished magnetic moment.

#### 2.4. Theoretical Analysis

CRO and SRO are exactly isostructural and isoelectronic, but different in magnetic ground states. The main difference is the strong octahedral tilting/rotation in CRO due to the much smaller ionic radius of  $\text{Ca}^{2+}$ . The octahedral tilting/rotation of CRO is nearly twice that of SRO.<sup>[47,48]</sup> It may be the reduced degree of octahedral tilting that results in the FM interfacial CRO phase. To confirm this inference, we performed DFT calculations for CRO layers with different degrees of octahedral tilting/rotation. CRO unit cells are constructed using experimental lattice constants under biaxial strain of LSAT and  $\beta_{\text{Ru-O-Ru}}$  angles varied from  $165^\circ$  to  $155^\circ$ . Details for DFT calculation are given in Experimental Section and Figure S6 (Supporting Information). As shown in Figure 5c, the non-spin-polarized density of states (DOS) at Fermi level  $N(E_{\text{F}})$  is significantly enhanced by the weakening of bond bending. It is 2.33, 2.42, 2.53, 2.66, and 2.72 states  $\text{eV}^{-1}$  corresponding to the  $\beta_{\text{Ru-O-Ru}}$  angles of  $155^\circ$ ,  $157^\circ$ ,  $160^\circ$ ,  $162^\circ$ , and  $165^\circ$ . This is consistent with previous works since a smaller octahedral tilting will reduce the degeneracy of  $t_{2\text{g}}$  bands thus enhance  $N(E_{\text{F}})$ .<sup>[37,47]</sup> The ferromagnetism in the ruthenates is generally understood based on the Stoner model with a Stoner criterion of  $IN(E_{\text{F}})$ , where  $I$  is the Stoner parameter. Obviously, a higher  $N(E_{\text{F}})$  is more energetically favorable to FM state. To determine the Stoner parameter, we conducted the fixed-spin moment calculations and obtained the magnetization dependence of the total energy ( $E$ ) for different  $\beta_{\text{Ru-O-Ru}}$  angles (see Figure S6, Supporting Information). Fitting the  $E$ - $M$  relation to the formula  $E = a_0 + \frac{a_2}{2}M^2 + \frac{a_4}{4}M^4$ , the Stoner parameter  $I$  then can be deduced from the coefficient  $a_2$ , adopting the relation  $a_2 = [1/N(E_{\text{F}}) - I]/2$ . The magnetization of model CRO can be determined from the valley position in the  $E$ - $M$  curves. Figure 5d shows the deduced  $IN(E_{\text{F}})$  and  $M$  as functions of  $\beta_{\text{Ru-O-Ru}}$ . When  $\beta_{\text{Ru-O-Ru}} = 160^\circ$ ,  $162^\circ$ , and  $165^\circ$ , CRO has a FM ground state since  $IN(E_{\text{F}}) > 1$ . The corresponding magnetizations are  $\approx 0.5$ ,  $\approx 0.6$ , and  $\approx 0.8 \mu_{\text{B}}/\text{f.u.}$ , showing a good agreement with experimental data. On the contrary, the ground state is PM when  $\beta_{\text{Ru-O-Ru}} = 155^\circ$  and  $157^\circ$ . This well explains why the interfacial FM only emerges in the first three CRO layers next to STO.

The effect of lattice strains is also considered in theoretical calculations. The calculated Stoner criterion for CRO on STO exhibits similar change with  $\beta_{\text{Ru-O-Ru}}$  angle as that for the SLs on LSAT, i.e., the FM phase is stable compared with PM phase when  $\beta_{\text{Ru-O-Ru}} > 160^\circ$  (see Table S1, Supporting Information).

### 3. Conclusion

In summary, an octahedron-tilting/rotation-caused FM phase in the CRO/STO SLs is revealed by both transport and magnetic measurements. This is the first report that a well FM ground state has been induced in heterostructures formed by two significantly symmetry-mismatched constituents, though neither of them has a magnetic order individually. The shared apical oxygen ions at orthorhombic-CRO/cubic-STO interface adjust the arrangement of the respective oxygen octahedral of CRO and STO, bring FM ground state into the interfacial CRO layers. Notably, an obvious advantage of such interfacial FM is it is retained in the ultrathin CRO layers with only 2 uc thickness, which is highly desired for designing spintronic materials/devices. In fact, the SL with 2 uc CRO sublayers also demonstrates the highest  $M_{\text{s}} \approx 0.7 \mu_{\text{B}}/\text{f.u.}$ . Our work indicates that integrating two perovskite oxides with different symmetries, thus different oxygen octahedron arrays, into heterostructures is a feasible way to obtain novel interfacial phases with unusual functionalities.

### 4. Experimental Section

**Sample Fabrication and Characterization:** High quality  $(\text{CRO}_n/\text{STO})_{10}$  SLs were epitaxially grown on (001)-oriented LSAT and STO substrates by the technique of pulsed laser deposition (KrF,  $\lambda = 248$  nm). The layer thickness varied from 2 to 10 uc for CRO and was fixed to 1 uc for STO. A bare CRO film with thickness of 50 uc was also prepared for comparison. During film growth, the substrate temperature was kept at  $670^\circ\text{C}$  and the oxygen pressure was set to 40 Pa. The adopted fluence of laser pulse was  $1.2 \text{ J cm}^{-2}$  and the repetition rate was 2 Hz. The deposition rate for the CRO and STO layers was carefully calibrated by the technique of small angle X-ray reflectivity (XRR, see Figure S1, Supporting Information). The crystal structure was determined by a high-resolution X-ray diffractometer (D8 Discover, Bruker) with the  $\text{Cu-K}\alpha$  radiation. The magnetic properties were measured by a Quantum Design vibrating sample magnetometer (VSM-SQUID) in the temperature range of 5–300 K, with the maximal magnetic field of 7 T. The magnetic field was applied along the out-of-plane direction of the (001) films. The transport measurements were performed in Quantum Design physical property measurement system (PPMS) with standard Hall bar geometry. Atomic-scale lattice images were recorded by a high-resolution scanning transmission electron microscope (STEM) with double  $C_5$  correctors (JEOL-ARM200F). To detect the distortion of oxygen octahedra, the annular bright-field (ABF) imaging mode was employed along with the high-angle annular dark-field (HAADF) imaging mode. Cross-sectional thin samples for STEM analysis were prepared using a dual-beam focused ion beam system along the [110] direction.

**First-Principles Calculations:** Density functional theory (DFT) calculations within the projected augmented-wave method as implemented in the Vienna ab initio Simulation Package (VASP) codes were used to investigate the magnetic ground state of CRO equipped with different octahedral distortions.<sup>[32–54]</sup> The local spin-density approximation of Ceperley–Alder parameterization was adopted for exchange-correlation energy.<sup>[55]</sup> A 500 eV energy cutoff was found to achieve numerical convergence. A  $k$ -point set of  $13 \times 13 \times 9$  Monkhorst–Pack mesh was found to be sufficient for the convergence of all properties computed here and was used in self-consistent calculations of the  $Pbnm$  unit cell.<sup>[56]</sup> For the electronic and fixed spin moment (FSM) calculations, a much denser  $k$ -point mesh of  $17 \times 17 \times 13$  were used. Atomic positions were optimized until the Hellmann–Feynman force on each atom was  $< 0.005 \text{ eV \AA}^{-1}$  and the electronic iteration was performed until the total energy difference between two steps was  $< 10^{-6} \text{ eV}$ .

## Supporting Information

Supporting Information is available from the Wiley Online Library or from the author.

## Acknowledgements

W.S., J.Z., and X.C. contributed equally to this work. This work was supported by the Science Center of the National Science Foundation of China (grant no. 52088101), the National Basic Research of China (grant nos. 2022YFA1403302, 2018YFA0305704 and 2019YFA0704904), the Project for Innovative Research Team of National Natural Science Foundation of China (project no. 11921004), the National Natural Science Foundation of China (grant nos. 11934016, 51972335, 12274443, and 12004022), the Strategic Priority Research Program (B) of the Chinese Academy of Sciences (no. XDB33030200), and the Key Program of the Chinese Academy of Sciences. The authors acknowledge Spallation Neutron Source Science Center for the PNR characterizations and Beamline BL08U1A in Shanghai Synchrotron Radiation Facility (SSRF) for the XAS characterizations.

## Conflict of Interest

The authors declare no conflict of interest.

## Data Availability Statement

The data that support the findings of this study are available in the supplementary material of this article.

## Keywords

CaRuO<sub>3</sub>, itinerant ferromagnetism, oxygen octahedra tilting, superlattices

Received: January 10, 2023

Revised: February 5, 2023

Published online: April 6, 2023

- [1] H. Takagi, H. Y. Hwang, *Science* **2010**, 327, 1601.
- [2] M. Imada, A. Fujimori, Y. Tokura, *Rev. Mod. Phys.* **1998**, 70, 1039.
- [3] E. Dagotto, *Science* **2005**, 309, 257.
- [4] Y. Tokura, N. Nagaosa, *Science* **2000**, 288, 462.
- [5] J. Heber, *Nature* **2009**, 459, 28.
- [6] G. R. Stewart, *Rev. Mod. Phys.* **2001**, 73, 797.
- [7] J. M. De Teresa, A. Barthelemy, A. Fert, J. P. Contour, F. Montaigne, P. Seneor, *Science* **1999**, 286, 507.
- [8] S. Okamoto, A. J. Millis, *Nature* **2004**, 428, 630.
- [9] P. Yu, J. S. Lee, S. Okamoto, M. D. Russell, M. Huijben, C. H. Yang, Q. He, J. X. Zhang, S. Y. Yang, M. J. Lee, Q. M. Ramasse, R. Erni, Y. H. Chu, D. A. Arena, C. C. Kao, L. W. Martin, R. Ramesh, *Phys. Rev. Lett.* **2010**, 105, 027201.
- [10] J. Matsuno, K. Ihara, S. Yamamura, H. Wadati, K. Ishii, V. V. Shankar, H.-Y. Kee, H. Takagi, *Phys. Rev. Lett.* **2015**, 114, 247209.
- [11] J. Matsuno, N. Ogawa, K. Yasuda, F. Kagawa, W. Koshibae, N. Nagaosa, Y. Tokura, M. Kawasaki, *Sci. Adv.* **2016**, 2, e1600304.
- [12] X. Liu, W. J. Song, M. Wu, Y. B. Yang, Y. Yang, P. P. Lu, Y. H. Tian, Y. W. Sun, J. D. Lu, J. Wang, D. Y. Yan, Y. G. Shi, N. X. Sun, Y. Sun, P. Gao, K. Shen, G. Z. Chai, S. P. Kou, C. W. Nan, J. X. Zhang, *Nat. Commun.* **2021**, 12, 5453.
- [13] S. W. Zeng, X. M. Yin, C. J. Li, C. S. Tang, K. Han, Z. Huang, Y. Cao, L. E. Chow, D. Y. Wan, Z. T. Zhang, Z. S. Lim, C. Z. Diao, P. Yang, A. T. S. Wee, S. J. Pennycook, A. Ariando, *Nat. Commun.* **2022**, 13, 743.
- [14] M. Gibert, P. Zubko, R. Scherwitzl, J. Íñiguez, J. M. Triscone, *Nat. Mater.* **2012**, 11, 195.
- [15] J. D. Hoffman, B. J. Kirby, J. Kwon, G. Fabbris, D. Meyers, J. W. Freeland, I. Martin, O. G. Heinonen, P. Steadman, H. Zhou, C. M. Schlepütz, M. P. M. Dean, S. G. E. teVelthuis, J.-M. Zuo, A. Bhattacharya, *Phys. Rev. X* **2016**, 6, 041038.
- [16] M. Caputo, Z. Ristic, R. S. Dhaka, T. Das, Z. Wang, C. E. Matt, N. C. Plumb, E. B. Guedes, J. Jandke, M. Naamneh, A. Zakharova, M. Medarde, M. Shi, L. Patthey, J. Mesot, C. Piamonteze, M. Radovic, *Adv. Sci.* **2021**, 8, 2101516.
- [17] M. W. Yoo, J. Tornos, A. Sander, L. F. Lin, N. Mohanta, A. Peralta, D. Sanchez-Manzano, F. Gallego, D. Haskel, J. W. Freeland, D. J. Keavney, Y. Choi, J. Stremper, X. Wang, M. Cabero, H. B. Vasili, M. Valvidares, G. Sanchez-Santolino, J. M. Gonzalez-Calbet, A. Rivera, C. Leon, S. Rosenkranz, M. Bibes, A. Barthelemy, A. Anane, E. Dagotto, S. Okamoto, S. G. E. teVelthuis, J. Santamaria, J. E. Villegas, *Nat. Commun.* **2021**, 12, 3283.
- [18] J. Nichols, X. Gao, S. Lee, T. L. Meyer, J. W. Freeland, V. Lauter, D. Yi, J. Liu, D. Haskel, J. R. Petrie, E.-J. Guo, A. Herklotz, D. Lee, T. Z. Ward, G. Eres, M. R. Fitzsimmons, H. N. Lee, *Nat. Commun.* **2016**, 7, 12721.
- [19] A. K. Jaiswal, D. Wang, V. Wollersen, R. Schneider, M. Le Tacon, D. Fuchs, *Adv. Mater.* **2022**, 34, 2109163.
- [20] P. W. Anderson, *Phys. Rev.* **1950**, 79, 350.
- [21] J. B. Goodenough, *Phys. Rev.* **1955**, 100, 564.
- [22] J. Kanamori, *J. Phys. Chem. Solids* **1959**, 10, 87.
- [23] S. Thomas, B. Kuiper, J. Hu, J. Smit, Z. Liao, Z. Zhong, G. Rijnders, A. Vailionis, R. Wu, G. Koster, J. Xia, *Phys. Rev. Lett.* **2017**, 119, 177203.
- [24] H. G. Lee, L. Wang, L. Si, X. He, D. G. Porter, J. R. Kim, E. K. Ko, J. Kim, S. M. Park, B. Kim, A. T. Shen Wee, A. Bombardi, Z. Zhong, T. W. Noh, *Adv. Mater.* **2020**, 32, 1905815.
- [25] W. Lin, L. Liu, Q. Liu, L. Li, X. Shu, C. Li, Q. Xie, P. Jiang, X. Zheng, R. Guo, Z. Lim, S. Zeng, G. Zhou, H. Wang, J. Zhou, P. Yang, Ariando, S. J. P., X. Xu, Z. Zhong, Z. Wang, J. Chen, *Adv. Mater.* **2021**, 33, 2101316.
- [26] K. Y. Meng, A. S. Ahmed, M. Bacani, A. O. Mandru, X. Zhao, N. Bagues, B. D. Esser, J. Flores, D. W. McComb, H. J. Hug, F. Yang, *Nano Lett.* **2019**, 19, 3169.
- [27] J. Lu, L. Si, Q. Zhang, C. Tian, X. Liu, C. Song, S. Dong, J. Wang, S. Cheng, L. Qu, K. Zhang, Y. Shi, H. Huang, T. Zhu, W. Mi, Z. Zhong, L. Gu, K. Held, L. Wang, J. Zhang, *Adv. Mater.* **2021**, 33, 21025.
- [28] L. Klein, L. Antognazza, T. H. Geballe, M. R. Beasley, A. Kapitulnik, *Phys. Rev. B* **1999**, 60, 1448.
- [29] R. Kennedy, R. Madden, P. Stampe, *J. Phys. D: Appl. Phys.* **2001**, 34, 1853.
- [30] D. L. Proffit, H. W. Jang, S. Lee, C. T. Nelson, X. Q. Pan, M. S. Rzchowski, C. B. Eom, *Appl. Phys. Lett.* **2008**, 93, 111912.
- [31] M. Schneider, V. Moshnyaga, P. Gegenwart, *Phys. Status Solidi B* **2010**, 247, 577.
- [32] Taniguchi, S., M. Ogawara, N. Fukuoka, S. Mizusaki, Y. Nagata, Y. Noro, H. Samata, *J. Magn. Magn. Mater.* **2009**, 321, 3335.
- [33] Z. Ali, M. Saghayezhian, Z. Wang, A. O'Hara, D. Shin, W. B. Ge, Y. T. Chan, Y. M. Zhu, W. D. Wu, S. T. Pantelides, J. D. Zhang, *npj Quantum Mater.* **2022**, 7, 108.
- [34] S. C. Shen, Z. L. Li, Z. J. Tian, W. D. Luo, S. Okamoto, P. Yu, *Phys. Rev. X* **2021**, 11, 021018.
- [35] V. Hardy, B. Raveau, R. Retoux, N. Barrier, A. Maignan, *Phys. Rev. B* **2006**, 73, 094418.
- [36] G. Cao, S. McCall, M. Shepard, J. E. Crow, R. P. Guertin, *Phys. Rev. B* **1997**, 56, 321.
- [37] I. I. Mazin, D. J. Singh, *Phys. Rev. B* **1997**, 56, 2556.



- [38] Y. Dai, Y. W. Zhao, L. Ma, M. Tang, X. P. Qiu, Y. Liu, Z. Yuan, S. M. Zhou, *Phys. Rev. Lett.* **2022**, *128*, 247202.
- [39] Z. Cui, A. J. Grutter, H. Zhou, H. Cao, Y. Dong, D. A. Gilbert, J. Wang, Y.-S. Liu, J. Ma, Z. Hu, J. Guo, J. Xia, B. J. Kirby, P. Shafer, E. Arenholz, H. Chen, X. Zhai, Y. Lu, *Sci. Adv.* **2020**, *6*, eaay0114.
- [40] R. Ramos, S. K. Arora, I. V. Shvets, *Phys. Rev. B* **2008**, *78*, 214402.
- [41] A. Annadi, Z. Huang, K. Gopinadhan, X. R. Wang, A. Srivastava, Z. Q. Liu, H. H. Ma, T. P. Sarkar, T. Venkatesan, Ariando, *Phys. Rev. B* **2013**, *87*, 201102(R).
- [42] A. T. Zayak, X. Huang, J. B. Neaton, K. M. Rabe, *Phys. Rev. B* **2008**, *77*, 214410.
- [43] Y. B. Chen, J. Zhou, F. X. Wu, W. J. Ji, S. T. Zhang, Y. F. Chen, Y. Y. Zhu, *Appl. Phys. Lett.* **2010**, *96*, 182502.
- [44] S. Tripathi, R. Rana, S. Kumar, P. Pandey, R. S. Singh, D. S. Rana, *Sci. Rep.* **2014**, *4*, 3877.
- [45] A. M. Glazer, *Acta Crystallogr., Sect. B: Struct. Crystallogr. Cryst. Chem.* **1972**, *28*, 3384.
- [46] P. Siwakoti, Z. Wang, M. Saghayezhian, D. Howe, Z. Ali, Y. Zhu, J. Zhang, *Phys. Rev. Mater.* **2021**, *5*, 114409.
- [47] H. T. Dang, J. Mravlje, A. Georges, A. J. Millis, *Phys. Rev. B* **2015**, *91*, 195149.
- [48] W. Bensch, H. W. Schmalke, A. Reller, *Solid State Ionics* **1990**, *43*, 171.
- [49] D. Kan, R. Aso, R. Sato, M. Haruta, H. Kurata, Y. Shimakawa, *Nat. Mater.* **2016**, *15*, 432.
- [50] D. Kan, R. Aso, H. Kurata, Y. Shimakawa, *J. Appl. Phys.* **2014**, *115*, 184304.
- [51] Y. Yuan, Y. Lu, G. Stone, K. Wang, C. M. Brooks, D. G. Schlom, S. B. Sinnott, H. Zhou, V. Gopalan, *Nat. Commun.* **2018**, *9*, 5220.
- [52] P. E. Blochl, *Phys. Rev. B* **1994**, *50*, 17953.
- [53] G. Kresse, J. Furthmuller, *Phys. Rev. B* **1996**, *54*, 11169.
- [54] G. Kresse, D. Joubert, *Phys. Rev. B* **1999**, *59*, 1758.
- [55] D. M. Ceperley, B. J. Alder, *Phys. Rev. Lett.* **1980**, *45*, 566.
- [56] H. J. Monkhorst, J. D. Pack, *Phys. Rev. B* **1976**, *13*, 5188.